



RESEARCH LETTER

10.1002/2017GL073029

Special Section:

Early Results: Juno at Jupiter

Key Points:

- We present the first comparison of Jupiter's auroras with an extended and complete set of near-Jupiter interplanetary data
- During compressions, the well-defined sector of Jupiter's emission and the dusk poleward region brightened, the latter pulsating
- The power emitted from the noon active region did not exhibit dependence on any interplanetary parameter, though the morphology changed

Supporting Information:

- Supporting Information S1

Correspondence to:

J. D. Nichols,
jdn4@le.ac.uk

Citation:

Nichols, J. D., et al. (2017), Response of Jupiter's auroras to conditions in the interplanetary medium as measured by the Hubble Space Telescope and Juno, *Geophys. Res. Lett.*, *44*, 7643–7652, doi:10.1002/2017GL073029.

Received 19 FEB 2017

Accepted 25 MAR 2017

Published online 14 AUG 2017

Response of Jupiter's auroras to conditions in the interplanetary medium as measured by the Hubble Space Telescope and Juno

J. D. Nichols¹ , S. V. Badman² , F. Bagenal³ , S. J. Bolton⁴ , B. Bonfond⁵ , E. J. Bunce¹ , J. T. Clarke⁶ , J. E. P. Connerney⁷ , S. W. H. Cowley¹ , R. W. Ebert⁴ , M. Fujimoto⁸, J.-C. Gérard⁵ , G. R. Gladstone⁴, D. Grodent⁵ , T. Kimura⁹ , W. S. Kurth¹⁰ , B. H. Mauk¹¹ , G. Murakami⁸ , D. J. McComas¹² , G. S. Orton¹³ , A. Radioti⁵, T. S. Stallard¹ , C. Tao¹⁴ , P. W. Valek⁴ , R. J. Wilson³ , A. Yamazaki¹³ , and I. Yoshikawa¹⁵ 

¹Department of Physics and Astronomy, University of Leicester, Leicester, UK, ²Department of Physics, Lancaster University, Lancaster, UK, ³Laboratory for Atmospheric and Space Physics, University of Colorado Boulder, Boulder, Colorado, USA, ⁴Southwest Research Institute, San Antonio, Texas, USA, ⁵Laboratory for Planetary and Atmospheric Physics, Institut d'Astrophysique et de Géophysique, Université de Liège, Liège, Belgium, ⁶Center for Space Physics, Boston University, Boston, Massachusetts, USA, ⁷Goddard Space Flight Center, Greenbelt, Maryland, USA, ⁸Institute of Space and Astronautical Science, Japan Aerospace Exploration Agency, Sagamihara, Japan, ⁹Nishina Center for Accelerator-Based Science, RIKEN, Hirosawa, Japan, ¹⁰Department of Physics and Astronomy, University of Iowa, Iowa City, Iowa, USA, ¹¹The Johns Hopkins University Applied Physics Laboratory, Laurel, Maryland, USA, ¹²Princeton Plasma Physics Laboratory, Princeton, New Jersey, USA, ¹³Jet Propulsion Laboratory, Pasadena, California, USA, ¹⁴Space Environment Laboratory, National Institute of Information and Communications Technology, Tokyo, Japan, ¹⁵Department of Complexity Science and Engineering, University of Tokyo, Kashiwa, Japan

Abstract We present the first comparison of Jupiter's auroral morphology with an extended, continuous, and complete set of near-Jupiter interplanetary data, revealing the response of Jupiter's auroras to the interplanetary conditions. We show that for ~1–3 days following compression region onset, the planet's main emission brightened. A duskside poleward region also brightened during compressions, as well as during shallow rarefaction conditions at the start of the program. The power emitted from the noon active region did not exhibit dependence on any interplanetary parameter, though the morphology typically differed between rarefactions and compressions. The auroras equatorward of the main emission brightened over ~10 days following an interval of increased volcanic activity on Io. These results show that the dependence of Jupiter's magnetosphere and auroras on the interplanetary conditions are more diverse than previously thought.

Plain Language Summary Jupiter's auroras (northern lights) are the brightest in the solar system, over a hundred times brighter than the Earth's. Auroras on Earth are driven by the solar wind, a million mile-per-hour stream of charged particles flowing away from the Sun, hitting the Earth's magnetic field, and stirring it around, but it is not known whether the solar wind causes any significant auroras on Jupiter. The main reason for this uncertainty is a lack of observations of the planet's auroras obtained while spacecraft have been near Jupiter and able to supply a full and continuous set of measurements of the solar wind and its accompanying magnetic field. In early mid-2016 Juno approached Jupiter, providing such an interplanetary data set, and we obtained over a month's worth of observations of Jupiter's auroras using the Hubble Space Telescope. We saw several solar wind storms, each causing auroral fireworks on Jupiter. We captured the most powerful auroras observed by Hubble to date, brightened main oval emissions, and flashing high-latitude patches of auroras during the solar wind storms. These results indicate that Jupiter's auroral response to the solar wind is more diverse than we previously have thought.

1. Introduction

The dynamics of Jupiter's magnetosphere are dominated by planetary rotation and the outflow of material from Io [see, e.g., *Khurana et al.*, 2004; *Clarke et al.*, 2004], and the nature of the solar wind interaction has long been debated [*Brice and Ioannidis*, 1970; *Southwood and Kivelson*, 2001; *Nichols et al.*, 2006; *Badman and Cowley*, 2007; *McComas and Bagenal*, 2007; *Cowley et al.*, 2008; *Delamere and Bagenal*, 2010]. Observationally,

©2017. The Authors.

This is an open access article under the terms of the Creative Commons Attribution License, which permits use, distribution and reproduction in any medium, provided the original work is properly cited.

the total power of the Jovian auroras in various wavelengths exhibits modulation by interplanetary conditions [Baron *et al.*, 1996; Pryor *et al.*, 2005; Clarke *et al.*, 2009; Badman *et al.*, 2016; Kita *et al.*, 2016; Kimura *et al.*, 2016; Dunn *et al.*, 2016], particularly increasing in some cases (not all) in response to expected solar wind compression regions characterized by overall high dynamic pressure and interplanetary magnetic field (IMF) strength.

The detailed morphological response of the far-ultraviolet auroras to the interplanetary medium has been examined previously using the Hubble Space Telescope (HST) and near-Jupiter spacecraft by Nichols *et al.* [2007, 2009a], the former study comparing HST images with Cassini flyby observations and the latter with New Horizons solar wind data and interplanetary measurements extrapolated from Earth orbit using a magneto-hydrodynamic model. These studies showed that in response to expected compression region onset the main emission sometimes brightened in the narrow region with System III longitude $\lambda_{III} > 180^\circ$ (usually observed in the dawn sector by HST), whereas, in contrast, the emission at smaller longitudes was neither bright nor well defined. However, intense arcs poleward of the main emission were observed during estimated compression regions for around 2 days following estimated compression region onset. An important limitation of those studies, however, was that they were hampered by relying on either limited HST or interplanetary observations or interplanetary data extrapolated from Earth that carried significant timing uncertainties. Further, those HST observations were obtained using either fixed ~ 100 s exposure times or time tag exposures of less than 5 min, both of which limit characterization of fast-varying auroral forms. In 2016 the NASA Juno spacecraft approached and entered into orbit around Jupiter (with orbit insertion on 5 July 2016), providing a full and continuous complement of near-Jupiter solar wind and IMF data. During this interval we observed Jupiter's FUV auroras using the HST Space Telescope Imaging Spectrograph (STIS) for 47 orbits from 16 May to 18 July, primarily using ~ 45 min time tag imaging exposures. In this paper we examine this unique combination of data in order to determine the response of Jupiter's auroras to conditions in the interplanetary medium. We show that Jupiter's auroral response to interplanetary conditions is more diverse than previously understood.

2. Data

2.1. Hubble Space Telescope Observations

We obtained 44 orbits of FUV time tag imaging and three orbits of FUV time tag spectroscopy using the HST/STIS Multi-Anode Microchannel Array detector over the interval May to July 2016. When imaging, we used the F25SRF2 filter, which admits H_2 Lyman and Werner bands. Observations were obtained with a cadence of roughly one orbit per 24 h (with some exceptions that contained two or three orbits) in three groups: days of year (DOYs) 137–159, 174–182, and 193–200. We concentrate here only on images of the northern auroras obtained during Juno approach, DOY 137–182, yielding 32 orbits. Raw images were extracted from the time tag data using integration and increment times of 30 s and 10 s, respectively, and images were then processed using the extensively used Boston University pipeline that has been discussed in detail previously [e.g., Clarke *et al.*, 2009; Nichols *et al.*, 2009a]. Here intensity was converted from counts to kR of total unabsorbed H_2 emission in the 70–180 nm bandwidth using the conversion factors of Gustin *et al.* [2012] (assuming a fiducial color ratio of 2.5; resultant powers are larger than those reported by Clarke *et al.* [2009] owing to the larger waveband considered). All images obtained in this program are shown in the supporting information (SI). Total emitted power and powers from different regions were extracted and corrected for viewing geometry using the method detailed by Nichols *et al.* [2009a], and times account for one-way light travel time.

2.2. Juno Interplanetary Data

We employ Juno interplanetary data presented and discussed in detail by McComas *et al.* [2017]. Specifically, we use 60 s resolution data in RTN coordinates from the fluxgate magnetometer (FGM) [Connerney *et al.*, 2017] and plasma moments computed using data from the Jovian Auroral Distributions Experiment (JADE) instrument [McComas *et al.*, 2013]. We compute the magnitude of the IMF in the plane perpendicular to the radial vector, i.e., $B_{\perp} = \sqrt{B_T^2 + B_N^2}$, and the clock angle θ_c of the IMF relative to the Jovian magnetic axis (thus with 0° indicating northward field, positive toward dawn), using the method detailed by Nichols *et al.* [2006]. We employ solar wind velocity v_{sw} and dynamic pressure p_{sw} measurements, using the latter to compute the magnetopause and bow shock stand-off distances, R_{mp} and R_{bs} , respectively, using the model of Joy *et al.* [2002]. The low-latitude dayside reconnection voltage ϕ_{LL} is then computed using the algorithm of Nichols *et al.* [2006], i.e., $\phi_{LL} = v_{sw} B_{\perp} L_0 \cos^4(\theta_c/2)$, where L_0 is the width of the channel in the solar wind that reconnects, taken to be $R_{mp}/2$.

We estimate the time of impact on the ionosphere using the method of *Nichols et al.* [2007], which considers three timescales. Briefly, these are (a) solar wind transport time given by the distance along the Sun-planet line between the position of the observed IMF phase front, calculated from Juno's position by using the mean Parker spiral angle of 11° , and R_{bs} as calculated above (b) the magnetosheath traversal time computed assuming a linear decrease in velocity from that just downstream of the shock, i.e., $0.26v_{sw}$ to that just upstream of the magnetopause, assumed to be 30 km s^{-1} , and (c) the time for disturbances to travel along outer magnetosphere field lines to the ionosphere via Alfvén waves. The overall lag/lead time varies between $\sim -5 \text{ h}$ (i.e., leading) and $\sim 3 \text{ h}$.

3. Results

The data discussed in section 2 are plotted in Figure 1, while selected representative HST images are shown in Figure 2. We first note from Figure 1a that the viewing geometry-corrected UV powers observed by HST are typically in the range $\sim 1\text{--}3 \text{ TW}$, with the notable exception of an event at $\sim 2 \text{ h}$ on DOY 142, during which HST observed a maximum UV power of $\sim 5.5 \text{ TW}$, the most powerful auroras observed by the telescope to date. For comparison, we also plot values obtained contemporaneously by the EXCEED instrument on the JAXA Hisaki satellite, provided by *Kimura and et al.* [2017]. The Hisaki powers are also corrected for viewing geometry and scaled to the same bandwidth of the HST values (see *Tao et al.* [2016] for further information). Hisaki UV powers broadly concur with HST observations, though with increased temporal coverage which indicated that the power continued to rise still further on DOY 142 to $\sim 8.5 \text{ TW}$ before dropping to $\sim 2.1 \text{ TW}$ at the time of the second HST observation on DOY 142 at $\sim 2130 \text{ h}$. Other notable enhancements of the total power up to values of $\sim 2 \text{ TW}$ occurred on DOYs 146, 151, 154, 175, 176, and 182, while a short-lived enhancement between HST orbits was observed by Hisaki on DOY 158.

The interplanetary data shown in Figures 1b–1g indicate that the field was B_T -dominated as expected at $\sim 5 \text{ AU}$ and that three solar wind compression regions were incident on Jupiter's magnetosphere during these intervals, separated by rarefaction regions of varying depth. The first compression was an interplanetary coronal mass ejection while the others were corotating interaction regions associated with crossings of the heliospheric current sheet. The observed times of the forward (reverse) shocks of these compressions are given by *McComas et al.* [2017], while the propagated times are $\sim 1000 \text{ h}$ on DOY 141 ($\sim 0000 \text{ h}$ on DOY 147), $\sim 1500 \text{ h}$ on DOY 149 ($\sim 0000 \text{ h}$ on DOY 155), and $\sim 0100 \text{ h}$ on DOY 173. Details about the interplanetary data can be found in *McComas et al.* [2017] but briefly, the compressions (colored blue in Figure 1) were characterized by high IMF strengths ($\sim 1\text{--}3 \text{ nT}$) and dynamic pressures ($\sim 2\text{--}5 \times 10^{-1} \text{ nPa}$), and accordingly low estimated magnetopause standoff distance $\sim 70 R_J$. The rarefactions observed were either shallow (colored cyan, with IMF strengths $\sim 0.5\text{--}0.7 \text{ nT}$ and dynamic pressures of order $\sim 10^{-2} \text{ nPa}$) or deep (colored yellow, with IMF strengths $\sim 0.1\text{--}0.2 \text{ nT}$ and dynamic pressures down to $\sim 2 \times 10^{-3} \text{ nPa}$). The estimated magnetopause standoff distance varied in response, with values between up to $\sim 130 R_J$. The solar wind velocity overall varied between $\sim 370 \text{ km s}^{-1}$ and $\sim 530 \text{ km s}^{-1}$ with large increases associated with the forward shocks of the compressions. Finally, the estimated low-latitude dayside reconnection voltage was generally larger during the compression regions and where the IMF turned northward, with values of $\sim 1\text{--}3 \text{ MV}$ in the compression regions, $\sim 0.4 \text{ MV}$ in the shallow initial rarefaction and $\sim 0.2 \text{ MV}$ in the deep rarefaction. It is also worth noting that an enhancement in Jupiter's sodium nebula was observed on DOY 140, coincidentally near the time of the observed first forward shock in this interval, (M. Yoneda, personal communication, 2017), and possibly associated with an eruption observed on Io on DOY 138 (K. de Kleer, personal communication, 2017).

It is first evident that all three forward shocks observed are accompanied by an enhancement of the total emitted UV power over $\sim 1\text{--}3 \text{ days}$ following the onset of the compression regions, and the extreme event on DOY 142 also follows a few hours after the sodium nebula enhancement. The power did not remain uniformly high during compressions; however, dropping to $\sim 1 \text{ TW}$ after a few days, and increasing toward the end of the first two compressions. On the basis of its morphology, discussed below, the brightening on DOY 182 was also likely associated with the onset of a compression region. We have calculated the Pearson correlation coefficients for the UV powers and interplanetary parameters smoothed with a boxcar width of one planetary rotation. A full table of results is shown in the SI, but here we restrict discussion to coefficients r_{xy} with significance $p < 0.05$, yielding in this case the correlation with B_\perp (r, p) $_{P_{UV}, B_\perp} = (0.45, 0.023)$ as the only significant value.

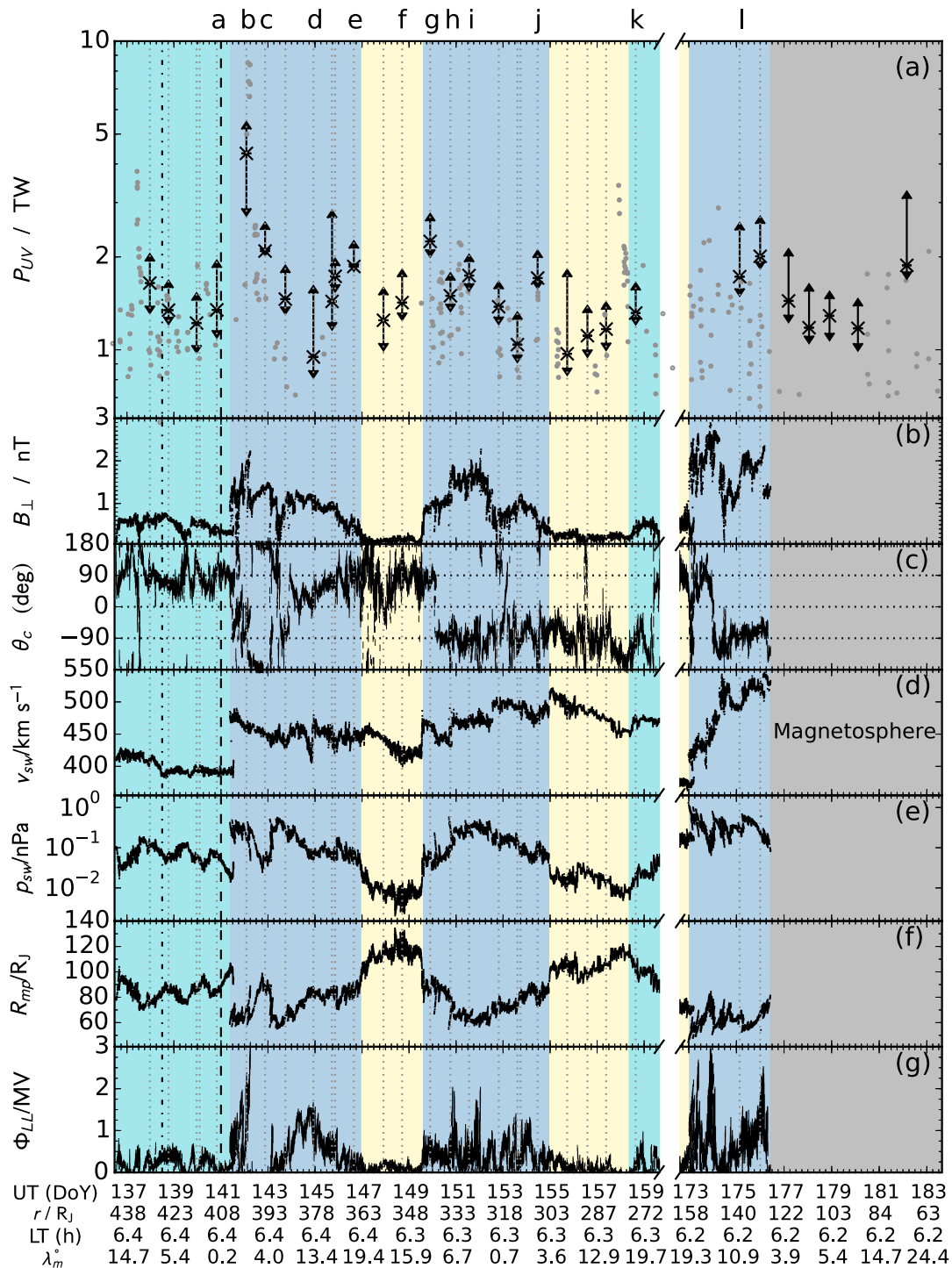


Figure 1. Plot showing auroral powers and interplanetary data versus UT at the ionosphere. We show (a) median and range of total UV powers P_{UV} in TW observed by HST in each orbit (black crosses with error bars) along with powers observed by Hisaki (gray points); (b) B_{\perp} in nT; (c) IMF clock angle θ_c in degrees along with horizontal dotted lines at 0 and $\pm 90^\circ$; (d) v_{sw} in km s^{-1} ; (e) p_{sw} in nPa; (f) R_{mp} in R_J ; and finally (g) Φ_{LL} in MV. Vertical dotted lines indicate the times of the HST observations. Also shown by the vertical dashed and dash-dotted lines are times of an observed eruption on Io and sodium nebula enhancement, respectively. The colors indicate different interplanetary conditions as discussed in the text, and the gray box indicates where Juno left the solar wind. The letters at the top correspond to the times of the images shown in Figure 2.

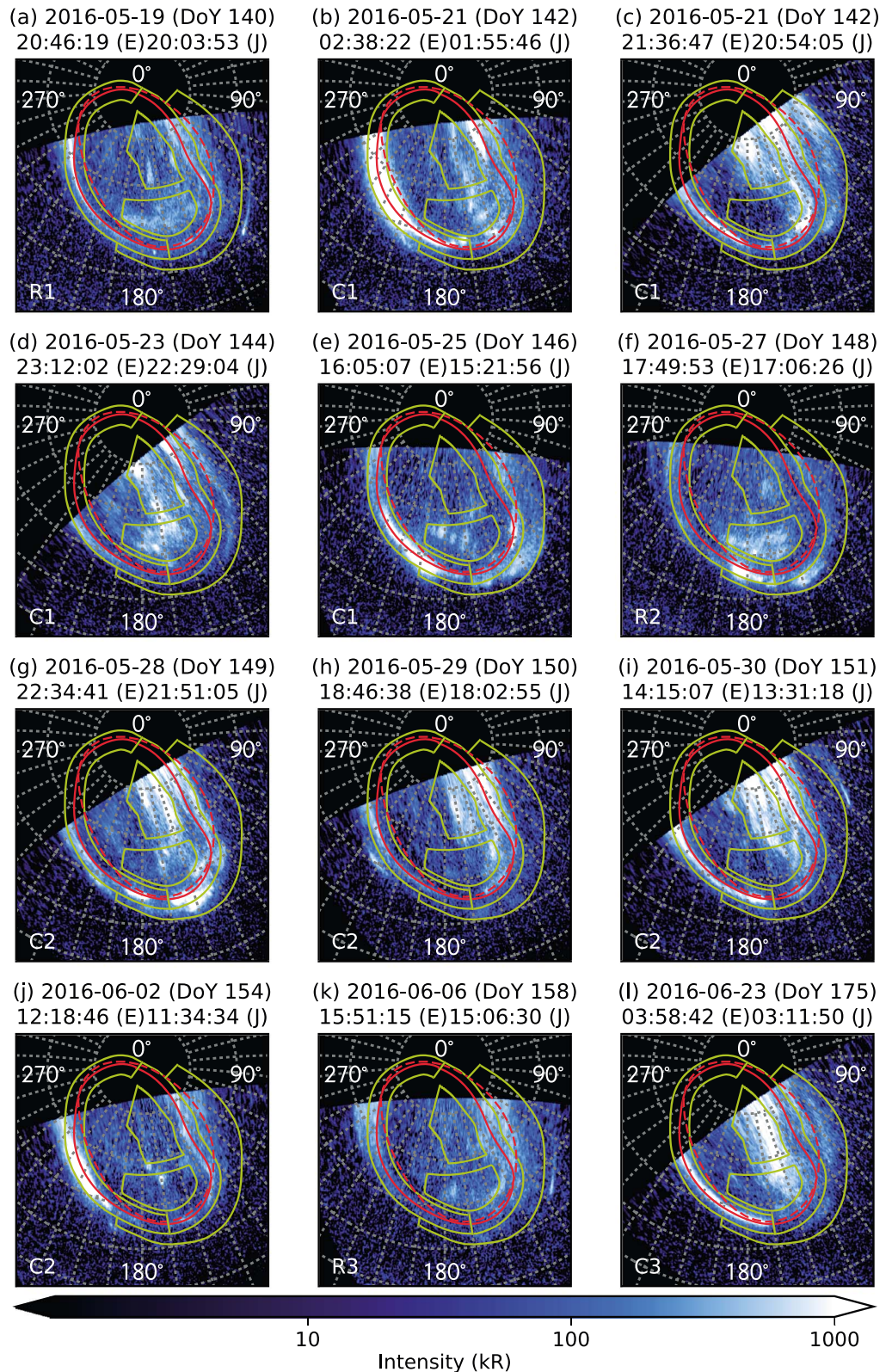


Figure 2. Representative projected images, shown with a $10^\circ \times 10^\circ$ graticule and $\lambda_{III} = 180^\circ$ directed toward the bottom. Red lines show the statistical oval for this program (solid) and the 30 R_J VIP4 oval [Connerney *et al.*, 1981, 1998] (dashed). The yellow lines denote the areas from which powers were extracted. Each image is labeled with the time of observation (E) and the time of emission (J). Labels in the bottom left refer to the interplanetary conditions, R1 denoting the first rarefaction, C2 the second compression, etc.

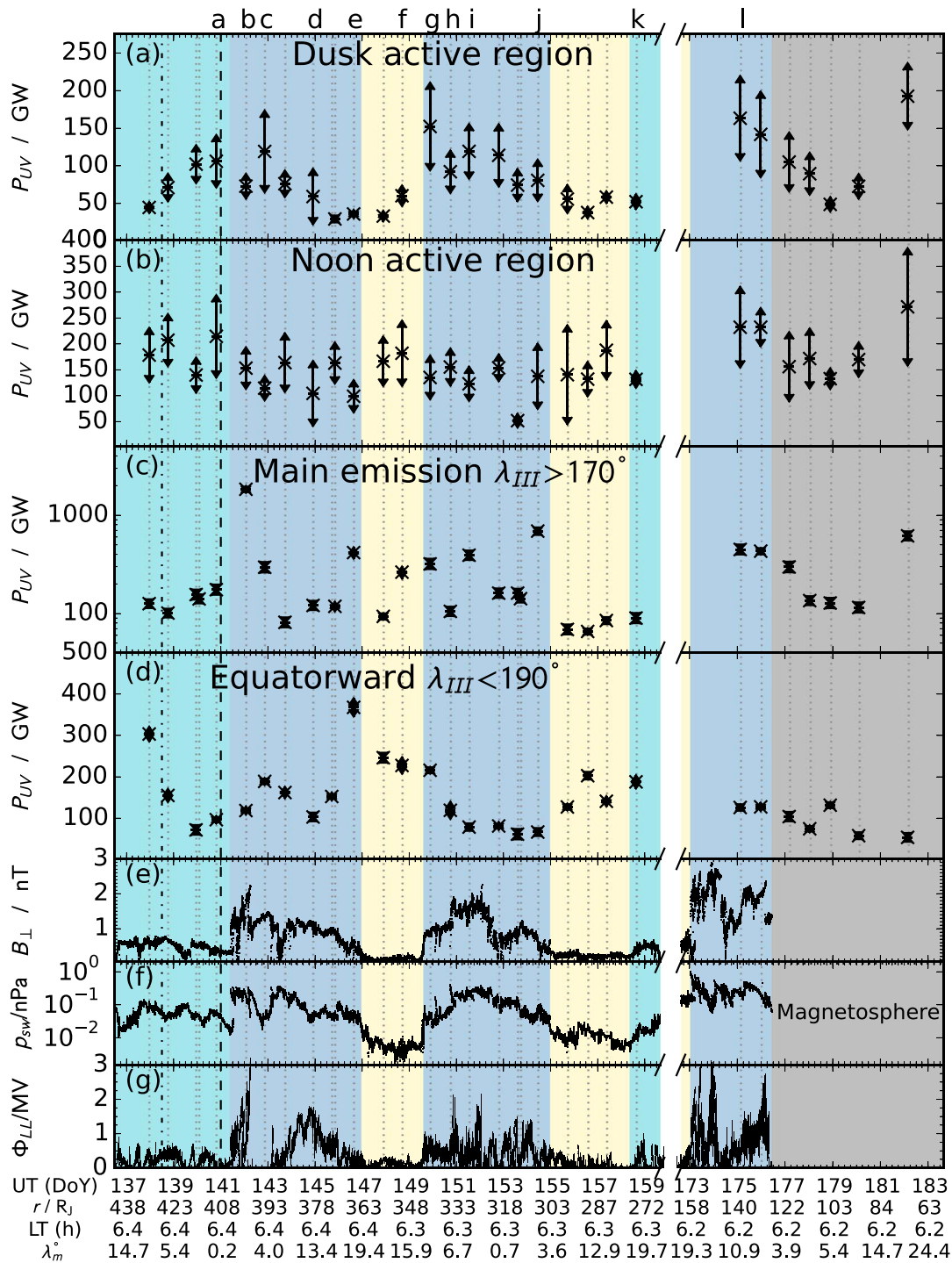


Figure 3. Plot showing powers from different auroral regions as labeled, in the same format as Figure 1. Note the log scale in Figure 3c.

Considering now the auroral morphology, representative images are shown in Figure 2, corresponding to the times labeled at the top of Figure 1. The powers from regions delimited by the yellow lines in Figure 2 are shown in Figure 3. These comprise two active regions observed poleward of the main emission, the well-defined portion of the main emission over $\lambda_{III} > 170^\circ$, and the equatorward region over $\lambda_{III} < 190^\circ$. Though the regions are fixed in λ_{III} , the well-defined main emission (WDME) region is typically observed by HST near dawn, the equatorward region near dusk, while the two poleward regions are in the dusk and noon sectors, hence termed here “dusk active region” (DAR) and “noon active region” (NAR), respectively.

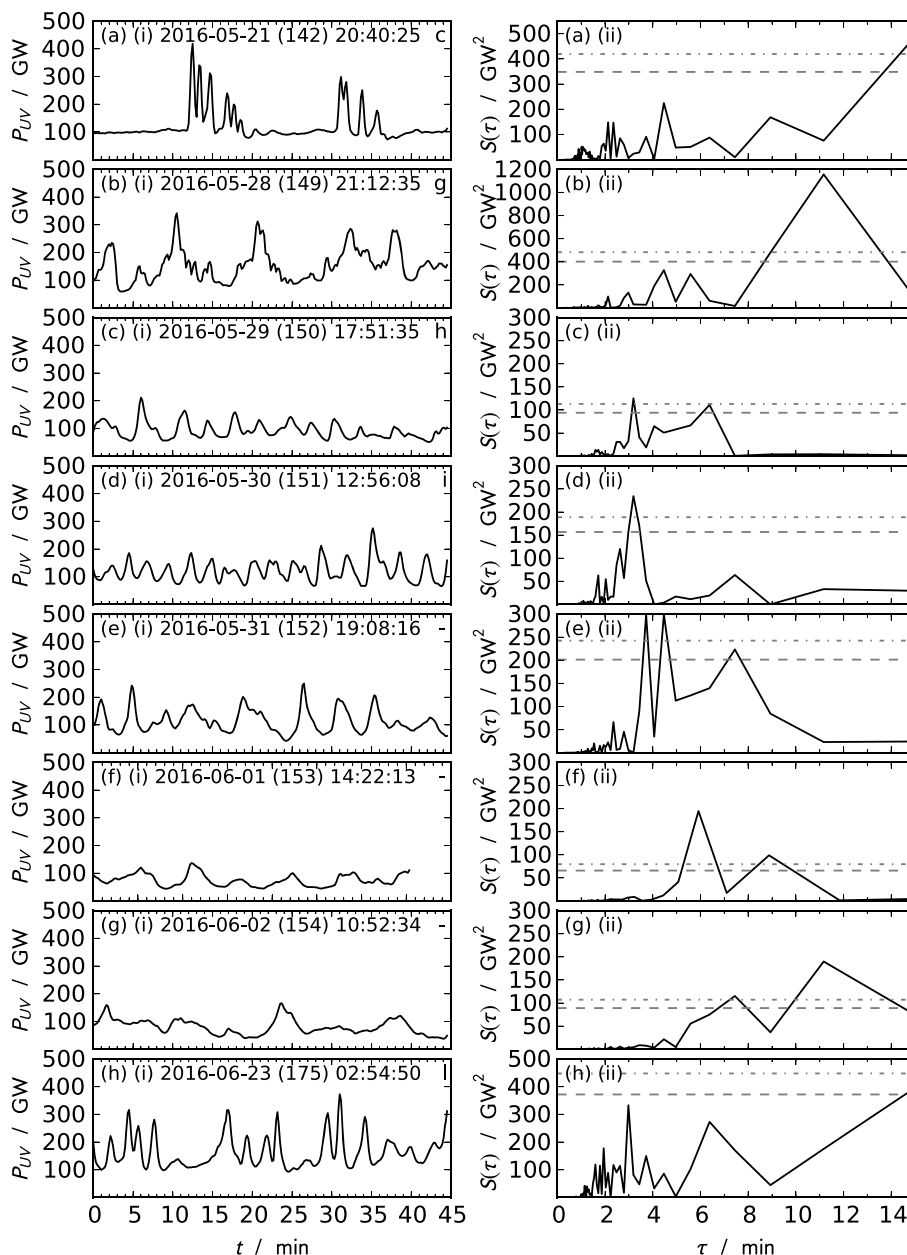


Figure 4. Plot showing (left column) time series of DAR powers obtained during selected orbits and (right column) power spectra $S(\tau)$ of the same, computed using fast Fourier transforms. Start times of the observations corrected for one-way light time are given, along with the corresponding image in Figure 2 if applicable. Times t and periods τ are both in units of minutes. Also shown are the 95% and 99% significance levels against the null hypothesis of white noise (gray dashed and dash-dotted lines, respectively).

We consider only the well-defined region of the main emission since the often unstructured nature of the auroras at smaller longitudes introduces ambiguity as to what is part of the main emission. We neglect low-latitude emission at $\lambda_{III} > 190^\circ$ to avoid contamination by bright, expanded dawn storm emissions. It is worth noting first that increased overall power in compressions arises from both intense few to a few tens of MR emission along the WDME and pulsed forms in the dusk and occasionally noon active regions. The DAR specifically exhibited bright, strongly pulsed emission during all three compressions and the initial shallow rarefaction conditions. The emission in this region typically (but not always) took the form of pulsing patches or arcs parallel to the main oval. A striking feature of such an arc observed on DOY 142 (Figure 2c) is that it marked the boundary between bright approximately few-hundred kR emissions on the duskside and an unusually

large dark polar region that was not evident in images obtained less than 20 h previously. The pulsed nature of the DAR emission is shown in Figure 4 for eight representative compression observations. These pulsations were either irregular and bursty (e.g., as in Figures 4a and 4h), or quasiperiodic, similar to those discussed recently by *Bonfond et al.* [2016], though we note that here we discuss power emitted in a fixed region, rather than identifying individual pulsating forms. As with those authors, however, we observe periods of ~ 3 min (e.g., Figures 4c and 4d) but also longer periods, such as ~ 6 min (Figure 4f) or ~ 11 min (Figures 4b and 4g). Interestingly, in the second compression, the peaks in the spectral power tended to broaden and move toward longer periods over DOYs 151–154 (Figures 4d–4g) as also evident in the overall powers in Figure 3a. In general, the DAR power broadly decreased during the compressions from large ~ 100 GW values to ~ 50 GW, and the DAR was typically less active during rarefactions. An exception to this occurred during the initial shallow rarefaction, when the DAR exhibited bright and variable emission, though more disordered and with fewer pulsed arc or patch structures. Overall, significant correlations are with B_{\perp} ($(r, p)_{P_{UV\text{DAR}} B_{\perp}} = (0.59, 0.002)$) and magnetopause size ($(r, p)_{P_{UV\text{DAR}} R_{\text{mp}}} = (-0.51, 0.010)$).

Turning now to the NAR, the powers for which are shown in Figure 3b, highly variable emission was observed during both rarefactions (e.g., Figures 2a and 2f) and compressions (e.g., Figure 2l), such that no significant correlations are observed with any interplanetary parameters. However, the morphology was somewhat different between the two cases, as exemplified by Figures 2f and 2l. In the rarefactions, the emission in the NAR comprised multiple, transient spots of emission extending throughout the NAR and often up into higher latitudes. Occasionally, the emission formed a poleward arc at noon, similar to the “inner ovals” discussed previously [*Pallier and Prangé*, 2001; *Grodent et al.*, 2003; *Nichols et al.*, 2009b; *Stallard et al.*, 2016]. In the compressions, the variable emission in the NAR typically comprised noonward extents of pulsating DAR emission though resembling more the rarefaction region morphology toward the end of the first compression.

Considering now the WDME, the emitted powers for which are shown in Figure 3c, the power did not stay uniformly high throughout the compression regions, decaying in the first compression from the ~ 1.8 TW dawn storm observed by HST (Figure 2b) to ~ 100 GW in ~ 1 day, and varying in the second between ~ 320 , 100, and 400 GW in Figures 2g, 2h, and 2i, before dropping back to ~ 160 GW. Toward the ends of both the first and second compressions, the region of the WDME exhibited high powers, though in these cases the emission was dominated by bright, patchy emission extending to lower latitudes in the case of Figure 2e (discussed further below), and a second dawn storm in the case of Figure 2j. The two observations during the third compression (e.g., Figure 2l) exhibited elevated powers of ~ 450 GW, but there was limited temporal coverage during this event. The power emitted from the WDME during the final observation on DOY 182 was high at ~ 600 GW, and this combined with the powerful, bursty ~ 200 GW DAR emission implies that these images were obtained during another compression. During the rarefactions, the WDME was typically dim as shown in e.g., Figures 2f and 2k. It is also interesting to note that there were unusually low intensities (a few tens of kR) on the duskside of the main oval in Figure 2f. Finally, it is worth mentioning that the statistical main oval for this program (see the SI for a table of coordinates) is $\sim 2^{\circ}$ equatorward of the 2007 statistical oval in the “kink” region.

We now consider the low longitude equatorward (LLEQ) emission, the powers for which are shown in Figure 3d. This region exhibited emission that varied significantly over the program, with values of ~ 50 – 350 GW, peaking on DOY 146. The emission was initially principally located in the kink region (Figure 2c), then taking the form of a secondary arc (Figure 2d), and the high powers on DOYs 146–149 corresponded to patchy emission of varying intensity, in some cases overlapping and extending down from the main emission, as discussed previously by *Radioti et al.* [2009], *Nichols et al.* [2009a], *Dumont et al.* [2015], and *Gray et al.* [2016]. Superficially, the equatorward powers seem to be enhanced in rarefaction regions though, with no significant correlations with any interplanetary parameter, this is not a robust result.

4. Discussion and Summary

We have presented the first set of HST observations made simultaneously with an extended and complete set of near-Jupiter interplanetary data, obtained by the Juno spacecraft. During the HST program Juno observed three compression regions in the interplanetary medium, interspersed by rarefaction regions of varying depth. We showed the following:

1. During the compressions (at least for ~ 1 – 3 days after each onset) the well-defined main emission usually observed by HST on the dawnside and a region poleward of the main emission on the duskside exhibited enhanced powers, with the latter comprising bursty or periodic patches and arcs parallel to the

main emission. This poleward dusk emission was also active during the shallow rarefaction at the start of the interval.

2. During the second compression, the dusk emission was quasiperiodic, with spectral peaks broadening and moving toward longer periods during the compression.
3. The noon active region exhibited transient emission during both rarefactions and compressions, though during compressions the emission was typically a noonward extension of the dusk active region emission, while during the rarefactions (and the later region of the first compression) the emission was either generally unstructured or formed an arc poleward of the main emission.
4. The auroras equatorward of the main emission at low longitudes exhibited a broad increase and decrease in power over an interval of ~ 10 days following the sodium nebula enhancement, initially exhibiting enhanced intensity in the dusk sector, then a prominent secondary arc, and finally bright patches of aurora overlapping the main emission.

The brightening of the WDME in response to compression region onset is confirmed and remains to be fully explained. Theoretical studies have indicated that the main oval should dim in response to compressions, with caveats concerning ionospheric response times [Southwood and Kivelson, 2001; Cowley *et al.*, 2007], though recently, Chané *et al.* [2017] have shown that at least the nightside main emission could brighten during compressions owing to enhanced magnetospheric asymmetries. Previous observations of small-scale poleward nightside flashing spots have been attributed to nightside reconnection [Grodent *et al.*, 2004], and the pulsating DAR emission is possibly a manifestation of larger-scale duskside/nightside compression-induced reconnection as part of the Vasyliunas or Dungey cycles. Additionally, the active DAR emissions during the initial shallow rarefaction is interesting and is either a response to ongoing activity at Io or the solar wind, noting that the IMF strength during this interval is significantly higher than that observed during the deep rarefaction. The extreme dawn storm/compression event observed on DOY 142 is likely a conflation of increased mass loading from Io coupled with a coincident onset of a compression region. Enhanced activity on Io is known to affect Jupiter's magnetosphere and auroras [Bonfond *et al.*, 2012; Yoneda *et al.*, 2010], and the brightening of the low-latitude emissions over the ~ 10 days following the sodium nebula enhancement possibly indicates the overall timescale for radial transport in Jupiter's magnetosphere [Louarn *et al.*, 2014; Gray *et al.*, 2016], though it is also consistent with the conclusions of Mauk *et al.* [1999] that clustered energetic particle injections are associated with solar wind rarefactions. The lack of a correlation between the NAR powers and any interplanetary parameters (e.g., v_{sw} or B_{\perp}) was surprising, but as noted above the morphology was typically distinct between compressions and rarefactions. It seems that the NAR region is neither driven simply by Kelvin-Helmholtz instability at the magnetopause nor reconnection according to the coupling function used here. Overall, these results evince a dependence of Jupiter's auroras on the interplanetary medium, which thus acts to trigger magnetospheric activity but that this is more complex than previously thought.

Acknowledgments

This work is based on observations made with the NASA/ESA Hubble Space Telescope (program GO 14105), obtained at STScI, which is operated by AURA, Inc. for NASA. Work at Leicester was supported by STFC Fellowship (ST/I004084/1) and STFC grant ST/K001000/1. S.V.B. was supported by STFC grant ST/M005534/1. J.T.C. was supported by grant HST-GO-14105.002-A from STScI to Boston University. Data are available at the MAST Archive (HST) and the NASA PDS Archive (Juno).

References

- Badman, S. V., and S. W. H. Cowley (2007), Significance of Dungey-cycle flows in Jupiter's and Saturn's magnetospheres, and their identification on closed equatorial field lines, *Ann. Geophys.*, *25*(4), 941–951.
- Badman, S. V., *et al.* (2016), Weakening of Jupiter's main auroral emission during January 2014, *Geophys. Res. Lett.*, *43*, 988–997, doi:10.1002/2015GL067366.
- Baron, R. L., T. Owen, J. E. P. Connerney, T. Satoh, and J. Harrington (1996), Solar wind control of Jupiter's H_3^+ auroras, *Icarus*, *120*(2), 437–442, doi:10.1006/icar.1996.0063.
- Bonfond, B., D. Grodent, J.-C. Gérard, T. S. Stallard, J. T. Clarke, M. Yoneda, A. Radioti, and J. Gustin (2012), Auroral evidence of Io's control over the magnetosphere of Jupiter, *Geophys. Res. Lett.*, *39*, L01105, doi:10.1029/2011GL050253.
- Bonfond, B., D. Grodent, S. V. Badman, J.-C. Gérard, and A. Radioti (2016), Dynamics of the flares in the active polar region of Jupiter, *Geophys. Res. Lett.*, *43*, 11,963–11,970, doi:10.1002/2016GL071757.
- Brice, N. M., and G. A. Ioannidis (1970), The magnetospheres of Jupiter and Earth, *Icarus*, *13*(2), 173–183, doi:10.1016/0019-1035(70)90048-5.
- Chané, E., J. Saur, R. Keppens, and S. Poedts (2017), How is the Jovian main auroral emission affected by the solar wind?, *J. Geophys. Res. Space Physics*, *122*, 1960–1978, doi:10.1002/2016JA023318.
- Clarke, J. T., D. Grodent, S. W. H. Cowley, E. J. Bunce, P. M. Zarka, J. E. P. Connerney, and T. Satoh (2004), Jupiter's aurora, in *Jupiter. The Planet, Satellites and Magnetosphere*, edited by F. Bagenal, T. E. Dowling, and W. B. McKinnon, pp. 639–670, Cambridge Univ. Press, Cambridge, U. K.
- Clarke, J. T., *et al.* (2009), Response of Jupiter's and Saturn's auroral activity to the solar wind, *J. Geophys. Res.*, *114*, A05210, doi:10.1029/2008JA013694.
- Connerney, J. E. P., M. H. Acuña, and N. F. Ness (1981), Modeling the Jovian current sheet and inner magnetosphere, *J. Geophys. Res.*, *86*, 8370–8384.
- Connerney, J. E. P., M. H. Acuña, N. F. Ness, and T. Satoh (1998), New models of Jupiter's magnetic field constrained by the Io flux tube footprint, *J. Geophys. Res.*, *103*(A6), 11,929–11,940, doi:10.1029/97JA03726.
- Connerney, J. E. P., *et al.* (2017), The Juno magnetic field investigation, *Space Sci. Rev.*, doi:10.1007/s11214-017-0334-z.

- Cowley, S. W. H., J. D. Nichols, and D. J. Andrews (2007), Modulation of Jupiter's plasma flow, polar currents, and auroral precipitation by solar wind-induced compressions and expansions of the magnetosphere: A simple theoretical model, *Ann. Geophys.*, *25*, 1433–1463.
- Cowley, S. W. H., S. V. Badman, S. M. Imber, and S. E. Milan (2008), Comment on "Jupiter: A fundamentally different magnetospheric interaction with the solar wind" by D. J. McComas and F. Bagenal, *Geophys. Res. Lett.*, *35*, L10101, doi:10.1029/2007GL032645.
- Delamere, P. A., and F. Bagenal (2010), Solar wind interaction with Jupiter's magnetosphere, *J. Geophys. Res.*, *115*, A10201, doi:10.1029/2010JA015347.
- Dumont, M., D. Grodent, A. Radioti, B. Bonfond, and J.-C. Gérard (2015), Jupiter's equatorward auroral features: Possible signatures of magnetospheric injections, *J. Geophys. Res. Space Physics*, *119*, 10,068–10,077, doi:10.1002/2014JA020527.
- Dunn, W. R., et al. (2016), The impact of an ICME on the Jovian X-ray aurora, *J. Geophys. Res. Space Physics*, *121*, 2274–2307, doi:10.1002/2015JA021888.
- Gray, R. L., S. V. Badman, and B. Bonfond (2016), Auroral evidence of radial transport at Jupiter during January 2014, *J. Geophys. Res. Space Physics*, *121*, 9972–9984, doi:10.1002/2016JA023007.
- Grodent, D., J. T. Clarke, J. H. Waite Jr., S. W. H. Cowley, J.-C. Gérard, and J. Kim (2003), Jupiter's polar auroral emissions, *J. Geophys. Res.*, *108*(A10), 1366, doi:10.1029/2003JA010017.
- Grodent, D., J.-C. Gérard, J. T. Clarke, G. R. Gladstone, and J. H. Waite Jr. (2004), A possible auroral signature of a magnetotail reconnection process on Jupiter, *J. Geophys. Res.*, *109*, A05201, doi:10.1029/2003JA010341.
- Gustin, J., B. Bonfond, D. Grodent, and J.-C. Gérard (2012), Conversion from HST ACS and STIS auroral counts into brightness, precipitated power, and radiated power for H₂ giant planets, *J. Geophys. Res.*, *117*, A07316, doi:10.1029/2012JA017607.
- Joy, S. P., M. G. Kivelson, R. J. Walker, K. K. Khurana, C. T. Russell, and T. Ogino (2002), Probabilistic models of the Jovian magnetopause and bow shock locations, *J. Geophys. Res.*, *107*(A10), 1309, doi:10.1029/2001JA009146.
- Khurana, K. K., M. G. Kivelson, V. M. Vasylunas, N. Krupp, J. Woch, A. Lagg, B. H. Mauk, and W. S. Kurth (2004), The configuration of Jupiter's magnetosphere, in *Jupiter. The Planet, Satellites and Magnetosphere*, edited by F. Bagenal, T. E. Dowling, and W. B. McKinnon, pp. 593–616, Cambridge Univ. Press, Cambridge, U. K.
- Kimura, T., et al. (2016), Jupiter's X-ray and EUV auroras monitored by Chandra, XMM-Newton, and Hisaki satellite, *J. Geophys. Res. Space Physics*, *121*, 2308–2320, doi:10.1002/2015JA021893.
- Kimura, T., et al. (2017), Auroral explosion at Jupiter observed by the Hisaki satellite and Hubble Space, *Geophys. Res. Lett.*, *44*, 4523–4531, doi:10.1002/2017GL072912.
- Kita, H., et al. (2016), Characteristics of solar wind control on Jovian UV auroral activity deciphered by long-term Hisaki EXCEED observations: Evidence of preconditioning of the magnetosphere?, *Geophys. Res. Lett.*, *43*, 6790–6798, doi:10.1002/2016GL069481.
- Louarn, P., C. P. Paranicas, and W. S. Kurth (2014), Global magnetodisk disturbances and energetic particle injections at Jupiter, *J. Geophys. Res. Space Physics*, *119*, 4495–4511, doi:10.1002/2014JA019846.
- Mauk, B. H., D. J. Williams, R. W. McEntire, K. K. Khurana, and J. G. Roederer (1999), Storm-like dynamics of Jupiter's inner and middle magnetosphere, *J. Geophys. Res.*, *104*(A10), 22,759–22,778, doi:10.1029/1999JA900097.
- McComas, D. J., and F. Bagenal (2007), Jupiter: A fundamentally different magnetospheric interaction with the solar wind, *Geophys. Res. Lett.*, *34*, L20106, doi:10.1029/2007GL031078.
- McComas, D. J., et al. (2013), The Jovian Auroral Distributions Experiment (JADE) on the Juno Mission to Jupiter, *Space Sci. Rev.*, doi:10.1007/s11214-013-9990-9.
- McComas, D. J., et al. (2017), Plasma environment at the dawn flank of Jupiter's magnetosphere: Juno arrives at Jupiter, *Geophys. Res. Lett.*, *44*, 4432–4438, doi:10.1002/2017GL072831.
- Nichols, J. D., S. W. H. Cowley, and D. J. McComas (2006), Magnetopause reconnection rate estimates for Jupiter's magnetosphere based on interplanetary measurements at ~5 AU, *Ann. Geophys.*, *24*, 393–406.
- Nichols, J. D., E. J. Bunce, J. T. Clarke, S. W. H. Cowley, J.-C. Gérard, D. Grodent, and W. R. Pryor (2007), Response of Jupiter's UV auroras to interplanetary conditions as observed by the Hubble Space Telescope during the Cassini flyby campaign, *J. Geophys. Res.*, *112*, A02203, doi:10.1029/2006JA012005.
- Nichols, J. D., J. T. Clarke, J.-C. Gérard, D. Grodent, and K. C. Hansen (2009a), Variation of different components of Jupiter's auroral emission, *J. Geophys. Res.*, *114*, A06210, doi:10.1029/2009JA014051.
- Nichols, J. D., J. T. Clarke, J.-C. Gérard, and D. Grodent (2009b), Observations of Jovian polar auroral filaments, *Geophys. Res. Lett.*, *36*, L08101, doi:10.1029/2009GL037578.
- Pallier, L., and R. Prangé (2001), More about the structure of the high latitude Jovian aurorae, *Planet. Space Sci.*, *49*(10–11), 1159–1173, doi:10.1016/S0032-0633(01)00023-x.
- Pryor, W. R., et al. (2005), Cassini UVIS observations of Jupiter's auroral variability, *Icarus*, *178*(2), 312–326, doi:10.1016/j.icarus.2005.05.021.
- Radioti, A., A. T. Tomas, D. Grodent, J.-C. Gérard, J. Gustin, B. Bonfond, N. Krupp, J. Woch, and J. D. Meniotti (2009), Equatorward diffuse auroral emissions at Jupiter: Simultaneous HST and Galileo observations, *Geophys. Res. Lett.*, *36*, L07101, doi:10.1029/2009GL037857.
- Southwood, D. J., and M. G. Kivelson (2001), A new perspective concerning the influence of the solar wind on the Jovian magnetosphere, *J. Geophys. Res.*, *106*(A4), 6123–6130, doi:10.1029/2000JA000236.
- Stallard, T. S., J. T. Clarke, H. Melin, S. Miller, J. D. Nichols, J. O'Donoghue, R. E. Johnson, J. E. P. Connerney, T. Satoh, and M. Perry (2016), Stability within Jupiter's polar auroral 'Swirl region' over moderate timescales, *Icarus*, *268*, 145–155, doi:10.1016/j.icarus.2015.12.044.
- Tao, C., T. Kimura, S. V. Badman, N. Andre, F. Tsuchiya, G. Murakami, K. Yoshioka, I. Yoshikawa, A. Yamazaki, and M. Fujimoto (2016), Variation of Jupiter's aurora observed by Hisaki/EXCEED: 2. Estimations of auroral parameters and magnetospheric dynamics, *J. Geophys. Res. Space Physics*, *121*, 4055–4071, doi:10.1002/2015JA021272.
- Yoneda, M., H. Nozawa, H. Misawa, M. Kagitani, and S. Okano (2010), Jupiter's magnetospheric change by Io's volcanoes, *Geophys. Res. Lett.*, *37*, L11202, doi:10.1029/2010GL043656.